

A LB-DF/FD Method for Particle Suspensions

Deming Nie^{1,2} and Jianzhong Lin^{1,2,*}

¹ State Key Laboratory of Fluid Power Transmission and Control, Zhejiang University, Hangzhou 310027, China.

² College of Metrology and Technology Engineering, China Jiliang University, Hangzhou 310018, China.

Received 30 September 2008; Accepted (in revised version) 10 July 2009

Communicated by Sauro Succi

Available online 23 September 2009

Abstract. In this paper, we propose a lattice Boltzmann (LB) method coupled with a direct-forcing fictitious domain (DF/FD) method for the simulation of particle suspensions. This method combines the good features of the LB and the DF/FD methods by using two unrelated meshes, namely, an Eulerian mesh for the flow domain and a Lagrangian mesh for the solid domain, which avoids the re-meshing procedure and does not need to calculate the hydrodynamic forces at each time step. The non-slip boundary condition is enforced by introducing a forcing term into the lattice Boltzmann equation, which preserves all remarkable advantages of the LBM in simulating fluid flows. The present LB-DF/FD method has been validated by comparing its results with analytical results and previous numerical results for a single circular particle and two circular particles settling under gravity. The interaction between particle and wall, the process of drafting-kissing-tumbling (DKT) of two settling particles will be demonstrated. As a manifestation of the efficiency of the present method, the settling of a large number (128) of circular particles is simulated in an enclosure.

AMS subject classifications: 76T20, 76-02, 76M28

Key words: Lattice Boltzmann method, direct-forcing fictitious domain method, particle suspension, numerical simulation.

1 Introduction

Many industrial processes involve transport of solid particles suspended in a fluid medium in the form of slurries, colloids, polymers, or ceramics, such as fluidized beds in chemical reactors, water treatment, paper formation, etc. It is therefore important to understand the macroscopic transport behavior of particle suspensions, which has attracted considerable attention in the past decades, both experimentally and numerically.

*Corresponding author. *Email addresses:* nieinhz@cjlu.edu.cn (D. Nie), linjz@cjlu.edu.cn (J. Lin)

Conventional numerical methods, such as the finite volume method (FVM) and finite element methods (FEM) are not very efficient in simulating particle suspensions. One of the main obstacles is the need of generating new, geometrically adapted grids, which is a very time-consuming task especially in three-dimensional flows. Another method for suspensions, Stokesian dynamics is proposed by Brady and Bossis [1], which is limited to suspensions with simple geometries such as spheres or spheroids in creeping flow.

More recently, the lattice-Boltzmann method (LBM) has been advocated as an effective computational tool for the simulation of complex flows [2,3]. Application of lattice Boltzmann (LB) method to simulate particles suspended in a viscous fluid was first proposed by Ladd [4,5]. However, Ladd's model requires fluid to cross the boundary of the suspended solid particle and occupy the entire domain such that the computational nodes inside and outside the solid particle are treated in an identical manner. Thus, this method is limited to the solid particles with density larger than the fluid density. Built on Ladd's framework, Aidun [6] proposed a new approach to overcome this drawback, which works well for analysis of suspended solid particles with any solid-to-fluid density ratio. Thereafter many relevant works [7–12] have been done to demonstrate that LBM is a robust and efficient method for simulating particulate flows containing a small or a large number of particles with spherical or complex geometry. However, in both Ladd's model and Aidun's model, the non-slip condition on the particle-fluid interface is treated by the bounce-back rule and the particle surface is represented by the boundary nodes, which are essentially a set of mid-points of the links between two fixed grids. If the first-order accurate Eulerian scheme is applied, this causes fluctuations on the computation of forces on the particle and further leads to fluctuations on the velocities of the particle. Despite of this drawback the LBM has still attracted many attentions [13–16] because of its several remarkable advantages, such as easy coding, no requirement of re-meshing procedure, and computational efficiency.

The direct-forcing fictitious domain (DF/FD) method, presented by Yu [17], is based on the distributed-Lagrange-multiplier/fictitious-domain (DLM/FD) method proposed by Glowinski et al. [18] and direct-forcing immersed boundary (DF/IB) method proposed by Fadlun et al. [19]. The key idea of the DLM/FD method is that the interior domains of the particles are filled with the same fluids as the surroundings and the Lagrange multiplier (physically a pseudo body force) is introduced to enforce the interior (fictitious) fluids to satisfy the constraint of rigid body motion. However, the calculation of the particle velocity and body-force is a little more involved. Consequently, the DF/FD method is more expensive than the DF/IB method [17] in which the non-slip condition is enforced by applying an equivalent forcing term into the Navier-Stokes equations. Thus, in DF/FD method, the body-force is treated in essentially the same way as the DF/IB method. As in the DLM/FD method, DF/FD method makes use of Eulerian lattice nodes for the fluid flow field and Lagrangian nodes to represent particles, and the body-force is distributed over the particle inner domain for the constraint that all inner fluids move as a rigid-body, which allows to update particle velocities explicitly without the need of computing the hydrodynamic force and torque on the particles [17], while in the DF/IB

method the body-force is only distributed on the particle boundary. As a result, the hydrodynamic force and torque have to be calculated explicitly.

In this work, we present the coupling of the DF/FD method to solve fluid-particle interactions and the LB method to solve fluid flow. The accuracy and robustness of the present method is demonstrated in simulations of sedimentation of a single particle in an infinite channel, sedimentation of a single particle in an enclosure, the DKT process of two circular particles, and sedimentation of 128 particles in an enclosure. It is noted that a number of works have addressed the coupling of the LBM and IB or DLM/FD method. Feng and Michaelides [20,21] proposed a LB-IB method coupling with a penalty method and a direct-forcing method, respectively. Niu et al. [22] proposed a multi-relaxation time LB model combined with immersed boundary method based on the momentum exchange approach. Shi and Lim [23] introduced a LB model integrated with distributed Lagrange multipliers/fictitious domain method to simulate fluid-elastic body interactions. Dupuis et al. [24] demonstrated an immersed boundary-lattice Boltzmann method for the simulation of the flow past an impulsively started cylinder. The purpose of this paper is to extend the LB method to fluid-particle interaction problems by using the DF/FD method.

2 Numerical model

2.1 Lattice-Boltzmann (LB) model

The fluid flow is solved by the LB method. The discrete LB equations of a single relaxation time model under external forces are described by

$$f_i(\mathbf{x} + \mathbf{e}_i \Delta t, t + \Delta t) - f_i(\mathbf{x}, t) = -\frac{1}{\tau} \left[f_i(\mathbf{x}, t) - f_i^{(0)}(\mathbf{x}, t) \right] + \frac{\omega_i \Delta t}{c_s^2} (\boldsymbol{\lambda} \cdot \mathbf{e}_i), \quad (2.1)$$

where $f_i(\mathbf{x}, t)$ is the distribution function on the i -direction microscopic velocity \mathbf{e}_i , $f_i^{(0)}(\mathbf{x}, t)$ is the equilibrium distribution function, $\boldsymbol{\lambda}$ is the external force, Δt is the time step of the simulation, τ is the relaxation time, c_s is the speed of sound and ω_i are weights related to lattice model. The fluid density ρ_f and velocity \mathbf{u} are determined by the distribution function

$$\rho_f = \sum_i f_i, \quad \rho_f \mathbf{u} = \sum_i f_i \mathbf{c}_i. \quad (2.2)$$

For the 2D 9-bit BGK model used here, the discrete velocity vectors are

$$\begin{aligned} \mathbf{e}_0 &= (0, 0), \\ \mathbf{e}_i &= \left(\cos\left(\frac{i-1}{2}\pi\right), \sin\left(\frac{i-1}{2}\pi\right) \right) \frac{\Delta x}{\Delta t}, \quad i=1 \sim 4, \\ \mathbf{e}_i &= \sqrt{2} \left(\cos\left(\frac{2i-9}{4}\pi\right), \sin\left(\frac{2i-9}{4}\pi\right) \right) \frac{\Delta x}{\Delta t}, \quad i=5 \sim 8, \end{aligned} \quad (2.3)$$

where Δx is the lattice spacing. The equilibrium distribution function is chosen as

$$f_i^{(0)}(\mathbf{x}, t) = \omega_i \rho_f \left[1 + \frac{3\mathbf{e}_i \cdot \mathbf{u}}{c^2} + \frac{9(\mathbf{e}_i \cdot \mathbf{u})^2}{2c^4} - \frac{3\mathbf{u}^2}{2c^2} \right], \quad (2.4)$$

where $c = \Delta x / \Delta t$, the speed of sound is defined as $c_s^2 = c^2 / 3$, and ω_i are chosen as the following values:

$$\begin{aligned} \omega_0 &= 4/9, \\ \omega_i &= 1/9, \quad i = 1 \sim 4, \\ \omega_i &= 1/36, \quad i = 5 \sim 8. \end{aligned} \quad (2.5)$$

By performing a Chapman-Enskog expansion and in the low Mach number limit, the macroscopic mass and momentum equations can be recovered

$$\frac{\partial \rho_f}{\partial t} + \nabla \cdot (\rho_f \mathbf{u}) = 0, \quad (2.6)$$

$$\frac{\partial (\rho_f \mathbf{u})}{\partial t} + \nabla \cdot (\rho_f \mathbf{u} \mathbf{u}) = -\nabla p + \nabla \cdot \left[v \left(\nabla (\rho_f \mathbf{u}) + \nabla (\rho_f \mathbf{u})^T \right) \right] + \lambda. \quad (2.7)$$

The kinematic viscosity can be expressed as $\nu = (2\tau - 1)(\Delta x)^2 / 6\Delta t$. Therefore, theoretically the LBGK model can only be used to simulate compressible flows in the incompressible limit.

2.2 Fictitious domain (FD) method

As in the DLM/FD method, the momentum equation for incompressible fluid flow is

$$\rho_f \frac{d\mathbf{u}}{dt} = \nabla \cdot \boldsymbol{\sigma} + \lambda \quad \text{in } \Omega \quad (\text{the whole domain}), \quad (2.8)$$

$$\mathbf{u} = \mathbf{U} + \boldsymbol{\omega}_s \times \mathbf{r} \quad \text{in } P(t) \quad (\text{the particle inner domain}), \quad (2.9)$$

where $\boldsymbol{\sigma} = -p\mathbf{I} + 2\mu\mathbf{S}$, with p the fluid pressure, μ the viscosity and \mathbf{S} the rate-of-strain tensor, λ is a pseudo body-force introduced over the particle inner domain to enforce the fictitious fluid to satisfy the rigid-body motion constraint which is zero outside the particle domain, and \mathbf{U} and $\boldsymbol{\omega}_s$ are the particle translational velocity and angular velocity, respectively. Note that (2.8) is applicable to incompressible fluid flow while (2.7) is applicable to compressible flows in the incompressible limit. For simplicity the following description is still based on (2.7), but there is a little difference in the implementation as shown in the following description.

The motion of the particle is governed by Newton's equation of motion as follows:

$$M \frac{d\mathbf{U}}{dt} = \mathbf{F}^H + \left(1 - \frac{1}{\rho_r} \right) M \mathbf{g} + \mathbf{F}^c, \quad (2.10)$$

$$\frac{d(\mathbf{J} \cdot \boldsymbol{\omega}_s)}{dt} = \mathbf{T}^H, \quad (2.11)$$

where M , \mathbf{J} are the particle mass, moment of inertia tensor, respectively; \mathbf{g} is the gravitational acceleration, and ρ_r is the solid-fluid density ratio, \mathbf{F}^c is the collision force acting on the particle by other particles and the wall when they come close to each other, \mathbf{F}^H and \mathbf{T}^H are the hydrodynamic force and torque on the particle, respectively, which are defined by

$$\mathbf{F}^H = \int_{\partial P} \mathbf{n} \cdot \boldsymbol{\sigma} ds, \quad (2.12)$$

$$\mathbf{T}^H = \int_{\partial P} \mathbf{r} \times (\mathbf{n} \cdot \boldsymbol{\sigma}) ds. \quad (2.13)$$

Here \mathbf{n} is the unit outward normal on the particle surface and \mathbf{r} is the position vector with respect to the particle mass center. From (2.8), (2.9), (2.12) and (2.13), we can obtain

$$\mathbf{F}^H = - \int_P \lambda d\Omega + M' \frac{d\mathbf{U}}{dt}, \quad (2.14)$$

$$\mathbf{T}^H = - \int_P \mathbf{r} \times \lambda d\Omega + \frac{d(\mathbf{J}' \cdot \boldsymbol{\omega}_s)}{dt}, \quad (2.15)$$

and

$$M' = \int_P \rho_f d\Omega, \quad \mathbf{J}' = \int_P \rho_f \mathbf{r} \times \mathbf{r} d\Omega, \quad (2.16)$$

which are determined numerically in the computations. M' and \mathbf{J}' can also be expressed as [17]:

$$M' = M / \rho_r, \quad \mathbf{J}' = \mathbf{J} / \rho_r. \quad (2.16')$$

The reason for using (2.16) instead of (2.16') is that the LB model used here is applied to simulate compressible flows in the incompressible limit. Numerical results have shown that a little difference exists between the two formulations, which would be discussed in Section 3.2.

Substituting (2.14) into (2.10), and (2.15) into (2.11) gives, respectively,

$$(M - M') \frac{d\mathbf{U}}{dt} = - \int_P \lambda d\Omega + \left(1 - \frac{1}{\rho_r}\right) M \mathbf{g} + \mathbf{F}^c, \quad (2.17)$$

$$\frac{d[(\mathbf{J} - \mathbf{J}') \cdot \boldsymbol{\omega}_s]}{dt} = - \int_P \mathbf{r} \times \lambda d\Omega. \quad (2.18)$$

2.3 Direct-forcing (DF) scheme

From Eq. (2.8), we can get

$$\lambda = \rho_f \frac{\partial \mathbf{u}}{\partial t} + \rho_f \mathbf{u} \cdot \nabla \mathbf{u} - \nabla \cdot \boldsymbol{\sigma} = \rho_f \frac{\partial \mathbf{u}}{\partial t} - \mathbf{rhs}. \quad (2.19)$$

The corresponding discrete form can be expressed as

$$\lambda^{n+1} = \rho_f \frac{\mathbf{u}^{n+1} - \mathbf{u}^n}{\Delta t} - \mathbf{rhs}^n = \rho_f \frac{\mathbf{u}^{n+1} - \mathbf{u}^*}{\Delta t} + \rho_f \frac{\mathbf{u}^* - \mathbf{u}^n}{\Delta t} - \mathbf{rhs}^n, \quad (2.20)$$

where \mathbf{u}^* is a temporary velocity which satisfies the momentum equation with zero body-force described as

$$\rho_f \frac{\mathbf{u}^* - \mathbf{u}^n}{\Delta t} - \mathbf{rhs}^n = 0. \quad (2.21)$$

Therefore, the forcing exerted on the Lagrangian points in the particle inner domain is

$$\lambda^{n+1} = \rho_f \frac{\mathbf{u}^{n+1} - \mathbf{u}^*}{\Delta t} = \rho_f \frac{\mathbf{U}^{n+1} + \boldsymbol{\omega}_s \times \mathbf{r} - \mathbf{u}^*}{\Delta t}. \quad (2.22)$$

The forcing is direct in the sense that the desired value of velocity is imposed directly in the particle inner domain without any dynamical process. The discrete formulations for (2.17) and (2.18) are

$$(M - M') \frac{\mathbf{U}^{n+1} - \mathbf{U}^n}{\Delta t} = - \int_P \lambda^{n+1} d\Omega + \left(1 - \frac{1}{\rho_r}\right) M \mathbf{g} + \mathbf{F}^{c^{n+1}}, \quad (2.23)$$

$$\frac{(\mathbf{J} - \mathbf{J}') \cdot (\boldsymbol{\omega}_s^{n+1} - \boldsymbol{\omega}_s^n)}{\Delta t} + \boldsymbol{\omega}_s^n \times [(\mathbf{J} - \mathbf{J}') \cdot \boldsymbol{\omega}_s^n] = - \int_P \mathbf{r} \times \lambda^{n+1} d\Omega. \quad (2.24)$$

Adding (2.22) into (2.23) and (2.24), respectively, gives

$$M \frac{\mathbf{U}^{n+1}}{\Delta t} = (M - M') \frac{\mathbf{U}^n}{\Delta t} + \left(1 - \frac{1}{\rho_r}\right) M \mathbf{g} + \int_P \rho_f \frac{\mathbf{u}^*}{\Delta t} d\Omega + \mathbf{F}^{c^{n+1}}, \quad (2.25)$$

$$\frac{\mathbf{J} \cdot \boldsymbol{\omega}_s^{n+1}}{\Delta t} = \frac{(\mathbf{J} - \mathbf{J}') \cdot \boldsymbol{\omega}_s^n}{\Delta t} - \boldsymbol{\omega}_s^n \times [(\mathbf{J} - \mathbf{J}') \cdot \boldsymbol{\omega}_s^n] + \int_P \rho_f \mathbf{r} \times \frac{\mathbf{u}^*}{\Delta t} d\Omega. \quad (2.26)$$

All the right-hand side terms of (2.25) and (2.26) are known except $\mathbf{F}^{c^{n+1}}$. A simple way to deal with it is to apply an explicit scheme with \mathbf{F}^{c^n} instead of $\mathbf{F}^{c^{n+1}}$. Besides, as shown from (2.25) and (2.26), the hydrodynamic force and torque exerted on the particle do not appear explicitly. As a result, it is unnecessary to calculate the hydrodynamic force and torque to update the particle motion.

The discrete quantity f in the Eulerian (\mathbf{x}_i) and Lagrangian (\mathbf{X}_l) frames are as follows:

$$f_L(\mathbf{X}_l) = \sum_i f_E(\mathbf{x}_i) \delta_\Delta(\mathbf{x}_i - \mathbf{X}_l), \quad f_E(\mathbf{x}_i) = \sum_l f_L(\mathbf{X}_l) \delta_\Delta(\mathbf{x}_i - \mathbf{X}_l) \Delta V_l, \quad (2.27)$$

where $\Delta V_l = V_p / N_l \cdot \Delta x^2$ for the 2D case ($\Delta V_l = V_p / N_l \cdot \Delta x^3$ for the 3D case), V_p is the particle volume (area for 2D case, e.g., $V_p = \pi D^2 / 4$ for a circular particle with diameter of D), N_l the number of Lagrangian nodes, and Δx the lattice spacing. The δ -function is defined by

$$\delta_\Delta(\mathbf{x}) = d_\Delta(x) \cdot d_\Delta(y) \cdot d_\Delta(z) \quad (2.28)$$

and

$$d_\Delta(r) = \begin{cases} 1 - \left| \frac{r}{\Delta x} \right|, & |r| < \Delta x, \\ 0, & \text{otherwise.} \end{cases} \quad (2.29)$$

2.4 LB-DF/FD method

The whole problem is decoupled into the fluid and solid particle sub-problems with the fractional step scheme, which includes the following steps:

-
- (a) Calculate $f^*(\mathbf{x}, t)$ from Eq. (2.1) without the body force and then \mathbf{u}^* from Eq. (2.2), which corresponds to solving Eq. (2.21).
 - (b) Based on Eqs. (2.25) and (2.26), calculate the particle translational velocity \mathbf{U} and the angular velocity $\boldsymbol{\omega}_s$.
 - (c) Update pseudo body-force $\boldsymbol{\lambda}^{n+1}$ inside the particle domain through Eq. (2.22).
 - (d) Introduce body-force $\boldsymbol{\lambda}^{n+1}$ into Eq. (2.1) and calculate $f(\mathbf{x}, t)$ without collision. Then the new ρ_f and \mathbf{u} are determined.
-

It is noted that the forcing term $\boldsymbol{\lambda}^n$ is retained to update $\boldsymbol{\lambda}^{n+1}$ in Eq. (2.22) with the purpose of higher accuracy and larger time step in [17]. For simplicity $\boldsymbol{\lambda}^n$ is set to be zero in the present numerical simulations, which is proved to be of good capability and high effectiveness.

2.5 Collision models

The collision model proposed by Wan and Turek [25] is used in the present numerical simulations. For particle-particle collisions, the repulsive force is determined as:

$$\mathbf{F}_{i,j}^P = \begin{cases} 0 & \text{for } d_{i,j} > R_i + R_j + \zeta, \\ \frac{1}{\varepsilon'_p} (\mathbf{X}_i - \mathbf{X}_j) (R_i + R_j - d_{i,j}) & \text{for } d_{i,j} \leq R_i + R_j, \\ \frac{1}{\varepsilon_p} (\mathbf{X}_i - \mathbf{X}_j) (R_i + R_j + \zeta - d_{i,j})^2 & \text{for } R_i + R_j \leq d_{i,j} \leq R_i + R_j + \zeta, \end{cases} \quad (2.30)$$

where R_i and R_j are the radius of the i th and j th particle, \mathbf{X}_i and \mathbf{X}_j are the coordinates of their mass centers, $d_{i,j} = |\mathbf{X}_i - \mathbf{X}_j|$ is the distance between their mass centers, ζ is the range of the repulsive force which is set to be Δx (lattice spacing) in the present numerical simulations, ε'_p and ε_p are small positive stiffness parameters for particle-particle collisions which are set to be 10^{-7} in the calculations. For the particle-wall collisions, the corresponding repulsive force reads,

$$\mathbf{F}_{i,j}^W = \begin{cases} 0 & \text{for } d'_i > 2R_i + \zeta, \\ \frac{1}{\varepsilon'_w} (\mathbf{X}_i - \mathbf{X}'_i) (2R_i - d'_i) & \text{for } d'_i \leq 2R_i, \\ \frac{1}{\varepsilon_w} (\mathbf{X}_i - \mathbf{X}'_i) (2R_i + \zeta - d'_i)^2 & \text{for } 2R_i \leq d'_i \leq 2R_i + \zeta, \end{cases} \quad (2.31)$$

where \mathbf{X}'_i is the coordinate vector of the center of the nearest imaginary particle located on the boundary and $d'_i = |\mathbf{X}_i - \mathbf{X}'_i|$, ε'_w and ε_w are small positive stiffness parameters for particle-wall collisions which are taken as $\varepsilon'_w = \varepsilon'_p/2$ and $\varepsilon_w = \varepsilon_p/2$ in the calculations.

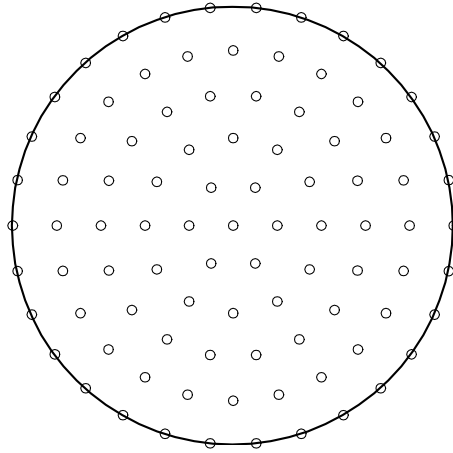
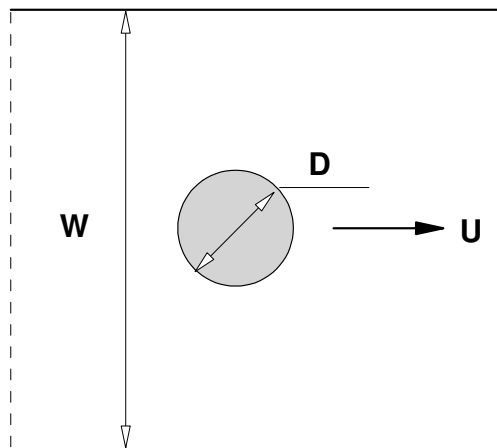


Figure 1: Arrangements of Lagrangian points for circular particles.

Figure 2: Schematic diagram of a circular particle with a constant velocity U in an infinite horizontal channel.

3 Numerical examples and discussions

3.1 Validation of LB-DF/FD method

The arrangement of Lagrangian points inside the circular particle proposed by Yu [17] is used, see Fig. 1, where one point is placed at the particle center, and $6i$ points on the i th ring for $i = 1, N_r$, with N_r being the number of the rings.

In order to demonstrate the ability of the present LB-DF/FD method for dealing with the fluid-particle interaction, a circular particle with a constant velocity U in an infinite channel is considered. A schematic diagram of the problem solved is depicted in Fig. 2.

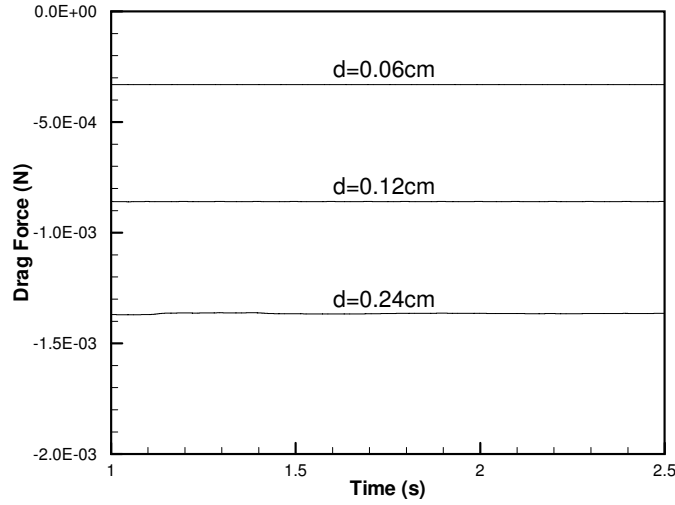


Figure 3: Drag force of the particle for three kinds of grid definition.

In this simulation, the computational parameters are summarized as follows: the lattice spacing is $\Delta x = 0.01\text{cm}$, the time step is $\Delta t = 1.0 \times 10^{-4}\text{s}$, the relaxation time is $\tau = 1.0$, the diameter of the particle is set to be $D = 0.06\text{cm}$, 0.12cm and 0.24cm , respectively, representing three kinds of grid definition ($D = 6\Delta x$, $12\Delta x$ and $24\Delta x$), the corresponding number of the rings is $N_r = 3$, 5 and 11 , the width of the channel is $W = 4D$, the fluid density is $\rho_f = 1.0\text{g/cm}^3$, the velocity is $U = 0.1\text{cm/s}$. As is known, the drag force of the particle in the channel keeps constant because of low Reynolds numbers.

Fig. 3 shows the results corresponding to the three kinds of grid definition. To assist clarity the results for $D = 0.12\text{cm}$ and 0.24cm have been displaced in the y direction by -5×10^{-4} and -1×10^{-3} , respectively. As shown, no fluctuations have been found in the results, even in the case of the coarsest grid ($D = 6\Delta x$), which demonstrates that better results can be obtained by the LB-DF/FD method than by previous LBMs with the first-order accurate Eulerian scheme. It should be mentioned that the smooth particle trajectories can also be obtained by the previous LBM proposed by Aidun et al. [6] if a second-order Verlet algorithm [26, 27] or a fourth-order Runge-Kutta scheme [6] is applied.

The next simulation is to validate the results of LB-DF/FD method by comparisons with an analytical solution. As shown in Fig. 4, a circular particle's sedimentation under gravitational force in an infinite channel is considered. The particle is initially set to be in the middle of the channel, released from rest at $t = 0$.

At low Reynolds numbers there is an analytical expression for the drag force on a circular particle settling in an infinite channel which can be described as [28]

$$F_d = 4\pi K\mu U, \quad (3.1)$$

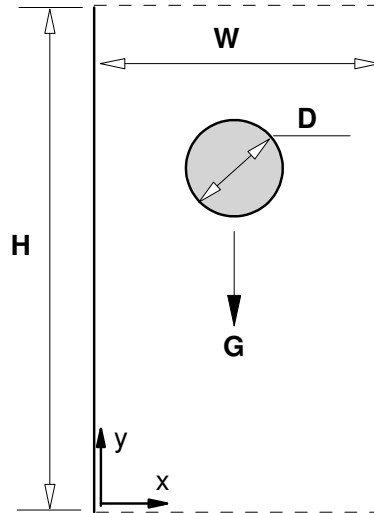


Figure 4: Schematic diagram of sedimentation of a circular particle under gravity in an infinite vertical channel.

where U is the particle settling velocity and K is defined by

$$K = \frac{1}{\ln W^* - 0.9157 + 1.7244(W^*)^{-2} - 1.7302(W^*)^{-4} + 2.4056(W^*)^{-6} - 4.5913(W^*)^{-8}}, \quad (3.2)$$

with $W^* = W/D$ the ratio of the channel width to the particle diameter. At steady state during sedimentation the gravitational force on the particle is balanced by the sum of the drag force and the buoyancy force. Thus the sedimentation velocity can be defined

$$U = \frac{D^2}{16K\mu} (\rho_f - \rho_s) g. \quad (3.3)$$

The corresponding computational parameters, the lattice spacing, time step, the fluid density and viscosity are the same as the above. Other parameters are: $\Omega = H \times W = 1.2\text{cm} \times 6\text{cm}$, $D = 0.24\text{cm}$, $\tau = 0.8$, $N_r = 11$. The particle is initially located at (0.6 cm, 3.0 cm). The inlet of the domain, where zero velocity is applied uniformly, is always $12.5D$ from the moving particle, whereas the downstream boundary is $12.5D$ from the particle. The normal derivative of velocity is set to zero at the downstream boundary. Non-equilibrium extrapolation method [29] has been adopted here for the inlet and outlet boundary conditions. In comparison with the scheme proposed by Aidun [6], the method of [29] is easier to be implemented. Moreover, it has been proved to be of second-order accuracy by the authors. In the simulation, as soon as the particle shifts by one lattice unit, the computational domain also moves by one lattice unit. This is done by removing one layer of fluid nodes at the downstream side of the system and adding one layer of

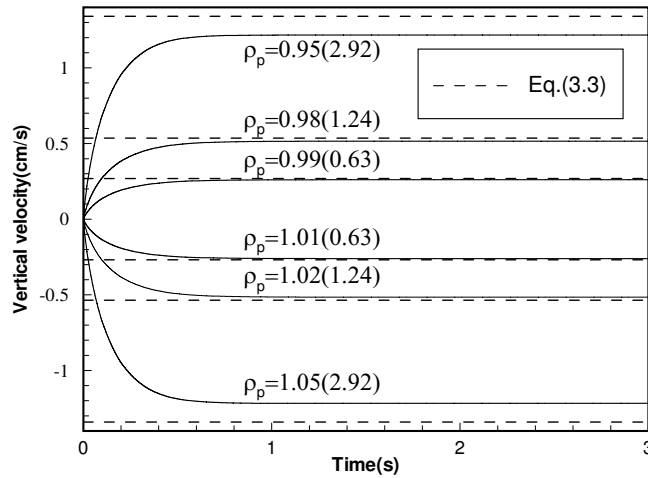


Figure 5: Time history of the sedimentation velocity of the particle at $W/D = 5$ for different particle densities. The numbers in the blankets are particle Reynolds number. The dash lines are theoretical results obtained by (3.3).

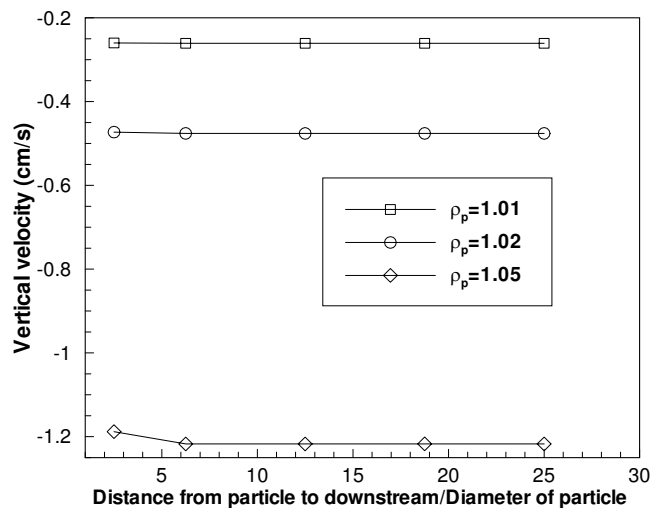


Figure 6: Effect of distance from moving particle to downstream on its settling velocity.

lattice nodes to the upstream side. In this way, the computational domain captures the relevant section of the infinite domain inside the channel.

Fig. 5 shows the time evolution of the settling velocities at two kinds of particle densities: 0.95, 0.98, 0.99 and 1.01, 1.02, 1.05. An excellent time independence of the particle velocity is observed when $Time > 0.9s$. The positive velocities for $\rho_p = 0.95, 0.98$ and 0.99 demonstrate that in the present LB-DF/FD method the solid-to-fluid density ratio can be less than or greater than one, which relaxes the assumption in LB model proposed by Ladd [4,5]. The numbers in the blankets are particle Reynolds number ($Re_p = \rho_f U_c D / \mu$,

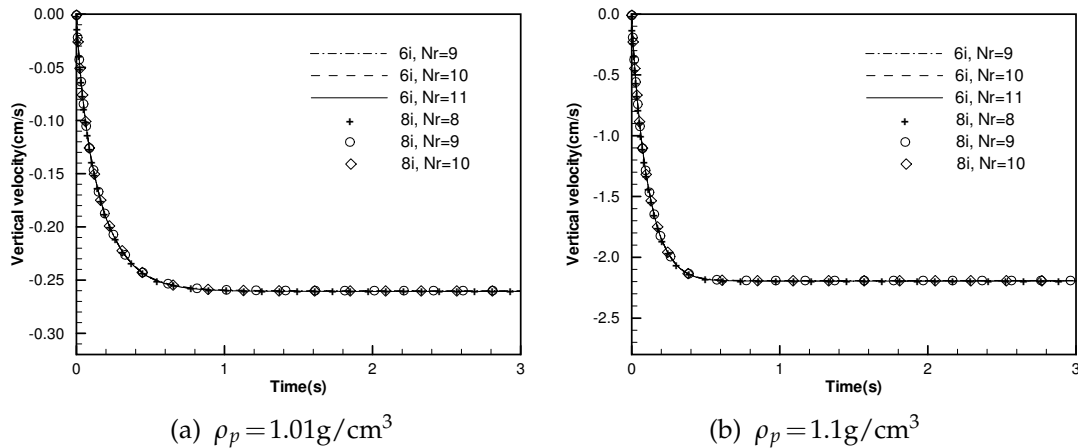


Figure 7: Time history of the sedimentation velocity of the particle for different numbers of Lagrangian nodes.

U_c is the settling velocity of particle). The dash line are theoretical results obtained by Eq. (3.3). A good agreement is observed when the particle Reynolds number is about 0.63 which is consistent with the low Reynolds number limit. The disagreement between numerical and analytical results is becoming obvious as the particle Reynolds number increases, as shown in Fig. 5. Fig. 6 shows that effect of the distance from moving particle to downstream on its settling velocity. As is shown, no effect is found when the distance is larger than $6.25D$, indicating that the present $12.5D$ used here is reasonable.

It should be remarked that the arrangement of Lagrangian nodes as shown in Fig. 1 is one of the possible ways to distribute Lagrangian points. Moreover, the number of Lagrangian nodes or the number of the rings used in the present work may not be optimal. In fact, there is no general theory or rule to determine these parameters. Numerical simulations suggest that the numbers of Lagrangian nodes can be chosen just to make ΔV_l not too large or too small, for the sake of numerical stability. Fig. 7 shows the time evolution of the settling velocities at different numbers of Lagrangian nodes for two kinds of arrangement, $N_r = 9, 10$ and 11 for "6i" and $N_r = 8, 9,$ and 10 for "8i", for $\rho_p = 1.01\text{g/cm}^3$ and 1.1g/cm^3 , respectively. Here "6i" refers to arrangement in which $6i$ points are on the i th ring as shown in Fig. 1, while "8i" refers to $8i$ points on the i th ring. The results indicate that the influences of the numbers of Lagrangian nodes and the arrangements of Lagrangian points are negligible. The value of ΔV_l is about 1.67, 1.37, 1.14 for $N_r = 9, 10,$ and 11 in "6i" arrangement and 1.56, 1.25, 1.03 for $N_r = 8, 9$ and 10 in "8i" arrangement. In general, the numbers of Lagrangian nodes chosen to make $\Delta V_l \approx 1$ may be a good choice, which is also stated by Yu [17].

3.2 Sedimentation of a circular particle in an enclosure

In this simulation, for convenience of comparison, the computational parameters are chosen as the same as those of Glowinski et al. [30] and Wang et al. [31], which are summa-

Table 1: Comparisons of the maximum Reynolds number during the particle sedimentation for $\rho_p = 1.25\text{g/cm}^3$ and $\mu = 0.1\text{g/cm}\cdot\text{s}$.

	Present		Wan and Turek [25]		Glowinski et al. [30]		Wang and Fan [31]		
Δx (cm)	1/100	1/200	1/48	1/96	1/192	1/256	1/72	1/144	1/256
Re_M	17.042	17.304	17.42	17.15	17.27	17.31	16.962	17.216	17.307

Table 2: Comparisons of the maximum Reynolds number during the particle sedimentation for $\rho_p = 1.5\text{g/cm}^3$ and $\mu = 0.01\text{g/cm}\cdot\text{s}$.

	Present		Wan and Turek [25]		Wang and Fan [31]			Uhlmann [32]
Δx (cm)	1/200	1/300	1/48	1/96	1/72	1/144	1/256	1/256
Re_M	487.28	489.91	442.19	465.52	502.37	503.26	503.38	495

rized as follows: $\Omega = 2\text{cm} \times 6\text{cm}$, $D = 0.25\text{cm}$, $\rho_p = 1.25\text{g/cm}^3$ and 1.5g/cm^3 , $\rho_f = 1.0\text{g/cm}^3$, $\mu = 0.1\text{g/cm}\cdot\text{s}$ and $0.01\text{g/cm}\cdot\text{s}$. The particle is initially located at the point (1cm, 4cm).

The maximum Reynolds number is defined as

$$\text{Re}_M = \text{Max} \left[\frac{\rho_p \cdot \sqrt{U_p^2 + V_p^2} \cdot D}{\mu} \right], \quad (3.4)$$

where U_p , V_p are the transversal and vertical velocity of mass center of the particle, respectively.

Table 1 shows the comparison of the maximum Reynolds number during the particle sedimentation for $\rho_p = 1.25\text{g/cm}^3$ and $\mu = 0.1\text{g/cm}\cdot\text{s}$ with previous related numerical results. Other computational parameters in this simulation are: $\Delta x = 0.01\text{cm}$, $\Delta t = 0.333 \times 10^{-4}\text{s}$, $\tau = 0.6$, $N_r = 8$ and $\Delta x = 0.005\text{cm}$, $\Delta t = 0.5 \times 10^{-4}\text{s}$, $\tau = 1.1$, $N_r = 18$. The present predicted maximum Reynolds numbers under different mesh sizes are in excellent agreement with those of Wan and Turek [25], Glowinski et al. [30] and Wang and Fan [31]. The Mach number for $\Delta x = 0.01\text{cm}$ and $\Delta x = 0.005\text{cm}$ is about 0.032 and 0.096, respectively. The incompressible limit is obviously valid.

Table 2 shows the comparison of the maximum Reynolds number during the particle sedimentation for $\rho_p = 1.5\text{g/cm}^3$ and $\mu = 0.01\text{g/cm}\cdot\text{s}$ with previous related numerical results. Other computational parameters in this simulation are: $\Delta x = 0.005\text{cm}$, $\Delta t = 0.5 \times 10^{-4}\text{s}$, $\tau = 0.56$, $N_r = 18$ and $\Delta x = 0.00333\text{cm}$, $\Delta t = 0.333 \times 10^{-4}\text{s}$, $\tau = 0.59$, $N_r = 26$. The present predicted maximum Reynolds numbers are in good agreement with those of Wang and Fan [31] and Uhlmann [32], but an apparent disagreement with Wan and Turek [25] is observed. The Mach number for $\Delta x = 0.005\text{cm}$ and $\Delta x = 0.00333\text{cm}$ is about 0.22, which is the maximal Mach number in the present simulations. Thus the fluid is nearly incompressible and the incompressible limit is still considered to be valid.

As shown in the numerical simulations, if Eq. (2.16') is adopted instead of using Eq. (2.16), the maximum Reynolds number is about 16.06 for $\rho_p = 1.25\text{g/cm}^3$ and

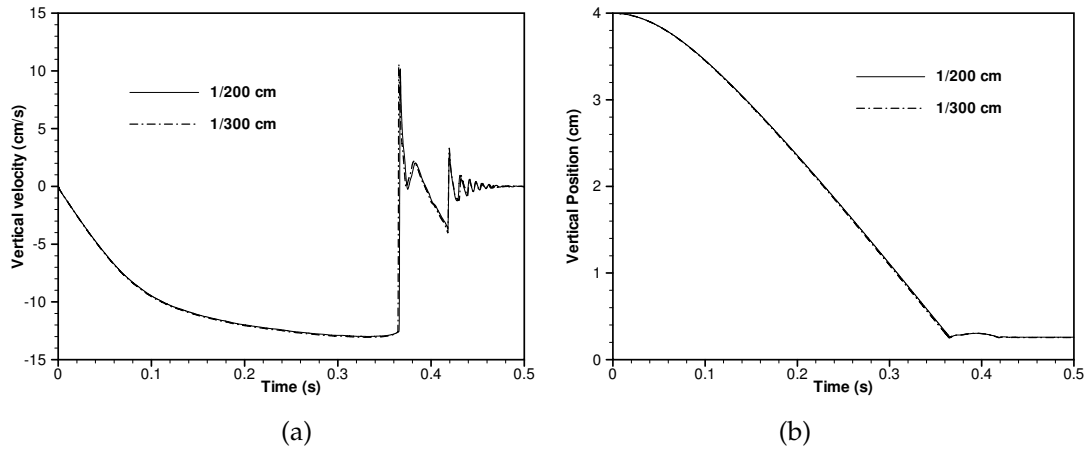


Figure 8: Time history of (a) vertical velocity, (b) vertical position of the particle for $\rho_p = 1.5\text{g/cm}^3$ and $\mu = 0.01\text{g/cm}\cdot\text{s}$.

$\mu = 0.1\text{g/cm}\cdot\text{s}$, and about 260 for $\rho_p = 1.5\text{g/cm}^3$ and $\mu = 0.01\text{g/cm}\cdot\text{s}$, which differs from the present result quantitatively. The reason is that even if the incompressible limit is valid, there is still difference between $\int_p \rho_f d\Omega$ and M/ρ_r , especially when the Mach number increases. Thus $\int_p \rho_f d\Omega$ cannot be replaced by M/ρ_r and should be defined by Eq. (2.27).

Fig. 8 shows the time evolution of the vertical velocity and the vertical position of the particle for $\rho_p = 1.5\text{g/cm}^3$ and $\mu = 0.01\text{g/cm}\cdot\text{s}$, respectively. As shown in Fig. 8(a), there is a little oscillation in the vertical velocity when the particle reaches the lower wall, which means a colliding force induced by the wall is added on the particle. When the particle rebounds back as shown in Fig. 8(b), the oscillation of the vertical position of the particle occurs. Finally the particle stays on the bottom. A little difference exists between Fig. 8(b) and the result of Wang and Fan [31]; the oscillation amplitude of the latter is larger.

Fig. 9 shows the corresponding instantaneous vorticity contours when the particle reaches the lower wall. A pair of symmetrical vortex behind the particle is observed in Fig. 9(a), and the vortex does not shed because of the limited computational and symmetrical initial conditions. While the particle moves to the region close to wall as shown in Fig. 9(b), another pair of vortices are created at the sides of the particle. The vortices are relatively thin and gradually grow up as the particle rebounds back as shown in Figs. 9(c) and (d). When the particle falls down again, the pair of vortices keep growing up and slowly move to its respective side wall along with the other pair of vortices which are obviously observed in Figs. 9(e) and (f).

3.3 Drafting-Kissing-Tumbling (DKT) process of two circular particles

The case of two circular particles sedimentation in a viscous fluid is also considered to validate the present LB-DF/FD method. An important phenomenon in this case is the well-known "Drafting-Kissing-Tumbling" (DKT) motion which has been studied exten-

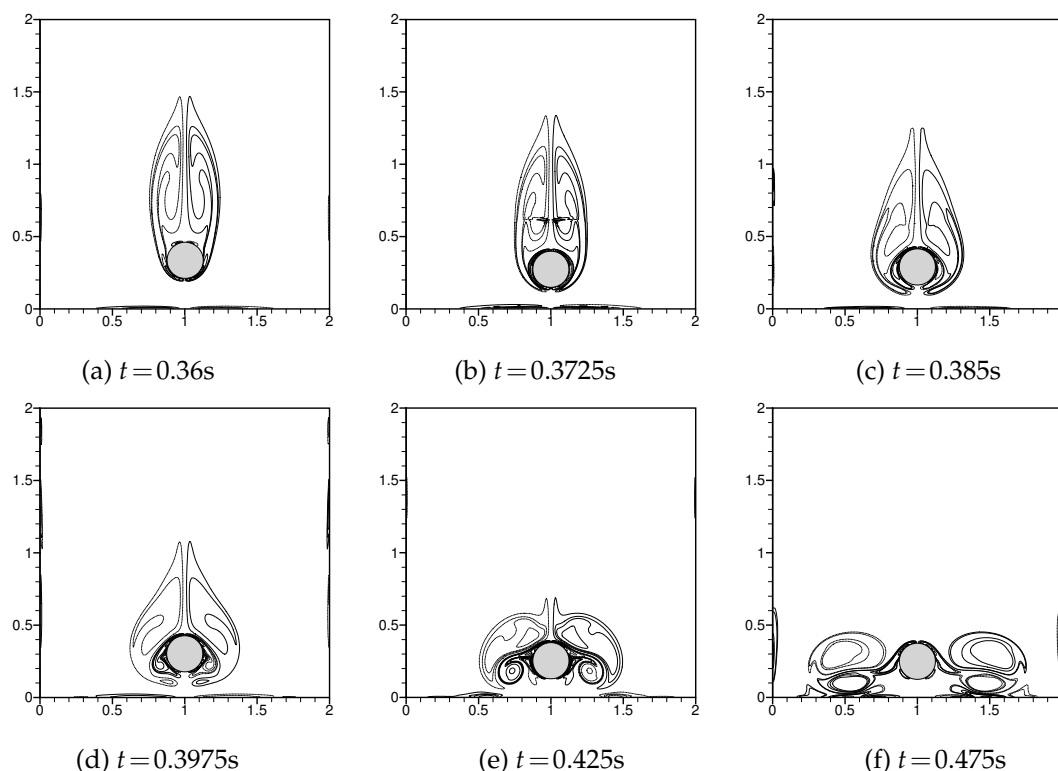


Figure 9: Instantaneous vorticity contours when particle reaches wall for $\rho_p = 1.5\text{g/cm}^3$ and $\mu = 0.01\text{g/cm}\cdot\text{s}$.

sively. The leading particle creates a wake of low pressure in which the trailing particle is caught, thus makes it fall faster than the leading one. This stage is called “Drafting”. Then the trailing particle of increased speed induces a kissing contact with the leading one in which the two particles form a long body with the line of center along the stream. This state, which is called “Kissing”, is unstable, and will be broken down at the last, after that the particles tumble.

The computational parameters are summarized as follows in this simulation: $\Omega = 2\text{cm} \times 6\text{cm}$, $\Delta x = 0.01\text{cm}$, $\Delta t = 0.333 \times 10^{-4}\text{s}$, $\tau = 0.6$, $D = 0.25\text{cm}$, $\rho_p = 1.5\text{g/cm}^3$, $\rho_f = 1.0\text{g/cm}^3$, $\mu = 0.1\text{g/cm}\cdot\text{s}$, $N_r = 8$. The particles are initially located at $(1 + 0.001\text{cm}, 4.5\text{cm})$ (leading particle), and $(1 - 0.001\text{cm}, 5\text{cm})$ (trailing particle).

Fig. 10 shows the positions of particles and vorticity contours of the flow during sedimentation at different time stages. Obviously, the DKT motion is reproduced. The instantaneous horizontal and vertical positions of the two particles are depicted in Fig. 11. It should be noted that, the cross observed in the vertical positions of the two particles, which suggests that the “Tumbling” is taking place for the two settling particles, does not indicate that the particles overlap because their instantaneous horizontal positions are different.

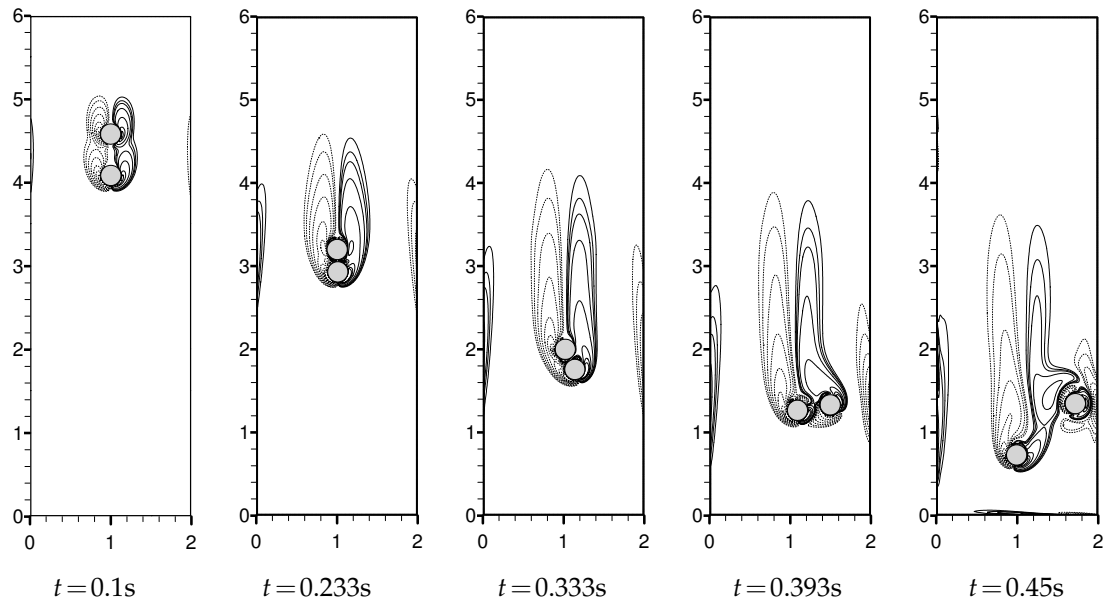


Figure 10: Sedimentation of two circular particles in a channel at different time for $\rho_p = 1.5\text{g/cm}^3$ and $\mu = 0.1\text{g/cm}\cdot\text{s}$.

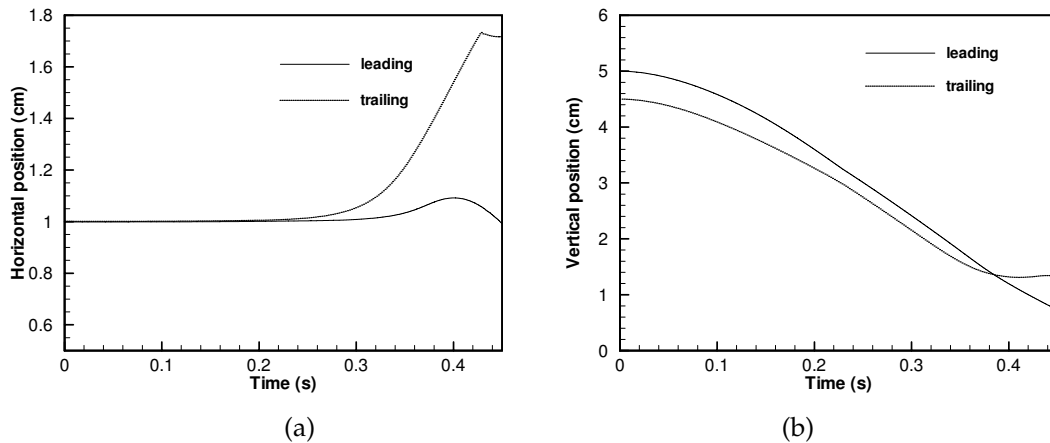


Figure 11: Time history of (a) horizontal positions, (b) vertical positions of the two particles for $\rho_p = 1.5\text{g/cm}^3$ and $\mu = 0.1\text{g/cm}\cdot\text{s}$.

3.4 Sedimentation of 128 circular particles in an enclosure

In order to further demonstrate the power of the LB-DF/FD method, sedimentation of 128 circular particles in an enclosure has been numerical simulated. The computational parameters are summarized as follows: $\Omega = 4.04\text{cm} \times 4.2\text{cm}$, $\Delta x = 0.02\text{cm}$, $\Delta t = 1.333 \times 10^{-4}\text{s}$, $\tau = 0.6$, $D = 0.20\text{cm}$, $\rho_p = 1.5\text{g/cm}^3$, $\rho_f = 1.0\text{g/cm}^3$, $\mu = 0.1\text{g/cm}\cdot\text{s}$, $N_r = 6$.

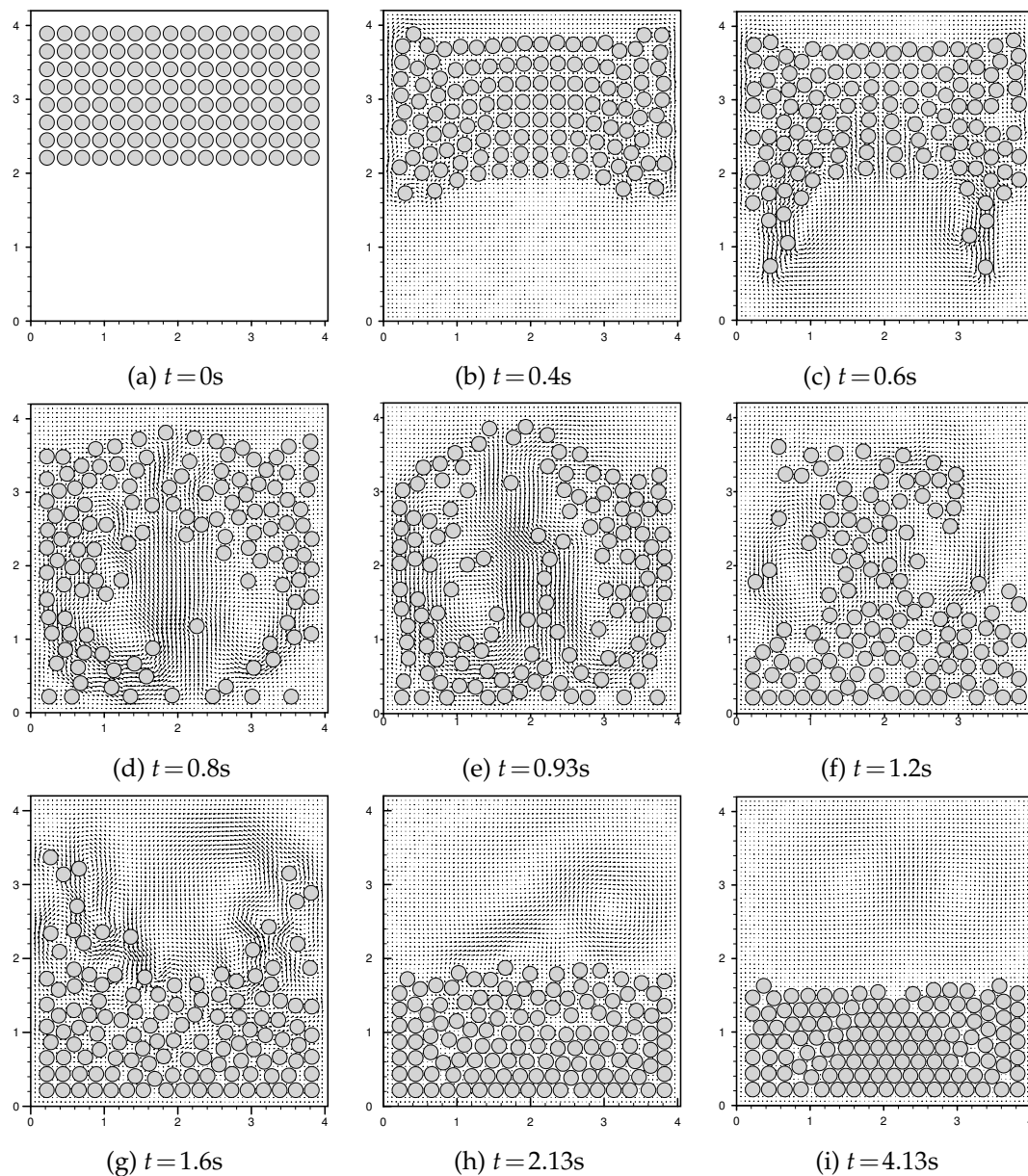


Figure 12: Sedimentation of 128 circular particles in an enclosure at different time.

There are 8 rows and in each row there are 16 particles. The 128 particles are placed at the top of the enclosure. The snapshots of the evolution and velocity fields for the sedimentation of 128 circular particles are shown in Fig. 12. The influence of the walls in hindering the closest particles is observed in Fig. 12(b), leading to the creation of two vortices close to the two top corners. As shown in Figs. 12(c)-(e), the particles near two

side walls fall down more quickly than those in the middle. The same phenomenon is reported in the literature [20, 31]. Due to the vortices in the two sides of the enclosure, some particles near the middle are held up by the fluid during the settling process, as shown in Fig. 12(f), and part of them are carried to the side walls settling down again, as shown in Fig. 12(g). Figs. 12(h)-(i) show the final stages of the settling process when all the particles have settled in the bottom of the enclosure. Obviously, there is some "packing" of the particles in the last two stages. The gaps between particles on the top are an indication of the slow process of particle packing. At the end, all the particles settle down and stay on the bottom of the enclosure.

4 Conclusion

The LB-DF/FD method, which combines the desired features of the Direct-forcing/fictitious method and the lattice Boltzmann method, has been proposed for simulating particle suspensions. This method makes use of two computational grids, the Eulerian one for the flow domain, and the Lagrangian one for the particles. The rigid body conditions are enforced by the direct-forcing scheme in which the desired value of velocity is imposed directly in the particle inner domain by introducing a pseudo body force to satisfy the constraint of rigid body motion, which is the key idea of fictitious domain method. The main advantages of the present method are that the re-meshing procedure is avoided and one does not need to calculate the hydrodynamic force and torque explicitly at each time step to update particle motion. Besides, it has been found that the present method preserves the merits of the LB method in simulating fluid flow.

The LB-DF/FD method has been validated by simulating four different cases (sedimentation of a single particle in an infinite channel, sedimentation of a single particle in an enclosure, the DKT process of two circular particles, sedimentation of 128 particles in an enclosure) and the results have been compared with those with other methods. The numerical evidences illustrated the capability and robustness of the present method for simulating particle suspensions.

Acknowledgments

This work was supported by the Scientific Project of Zhejiang Province of China (No. 2008C01024-4). We are thankful to Dr. Zhaosheng Yu for helpful discussions and suggestions on the Direct-forcing/fictitious domain method.

References

- [1] J. F. Brady and G. Bossis, Stokesian dynamics, *Annu. Rev. Fluid Mech.*, 20 (1988), 111–157.
- [2] R. Benzi, S. Succi and M. R. Vergassola, The lattice Boltzmann equation: theory and applications, *Phys. Rep.*, 222 (1992), 145–197.

- [3] S. Y. Chen and G. D. Doolen, Lattice Boltzmann method for fluid flows, *Annu. Rev. Fluid Mech.*, 30 (1998), 329–364.
- [4] A. J. C. Ladd, Numerical simulations of particulate suspensions via a discretized Boltzmann equation Part I. Theoretical foundation, *J. Fluid Mech.*, 271 (1994), 285–310.
- [5] A. J. C. Ladd, Numerical simulations of particulate suspensions via a discretized Boltzmann equation. Part II. Numerical results, *J. Fluid Mech.*, 271 (1994), 311–339.
- [6] C. K. Aidun, Y. N. Lu and E. J. Ding, Direct analysis of particulate suspensions with inertia using the discrete Boltzmann equation, *J. Fluid Mech.*, 373 (1998), 287–311.
- [7] D. W. Qi, Lattice-Boltzmann simulations of particles in non-zero-Reynolds-number flows, *J. Fluid Mech.*, 385 (1999), 41–62.
- [8] A. J. C. Ladd and R. Verberg R, Lattice-Boltzmann simulation of particle-fluid suspensions, *J. Stat. Phys.*, 104 (2001), 1191–1251.
- [9] Z. G. Feng and E. E. Michaelides, Hydrodynamic force on spheres in cylindrical and prismatic enclosures, *Int. J. Multiphase Flow*, 28 (2002), 479–496.
- [10] J. Z. Lin, X. Shi and Z. J. You, Effects of the aspect ratio on the sedimentation of a fiber in Newtonian fluids, *J. Aerosol Science*, 34 (2003), 909–921.
- [11] J. Z. Lin, X. M. Shao, X. Shi and Z. S. Yu, Study on the interaction of sedimenting cylindrical particles in still fluid, *Acta Mechanica Sinica*, 20 (2004), 33–45.
- [12] J. Z. Lin, Y. L. Wang and A. O. James, Sedimentation of Rigid Cylindrical Particles with Mechanical Contacts, *Chinese Physics Letter*, 22 (2005), 628–631.
- [13] X. B. Nie, G. D. Doolen and S. Y. Chen, Lattice-Boltzmann Simulations of Fluid Flows in MEMS, *J. Stat. Phys.*, 107 (2002), 279–289.
- [14] X. Shi, J. Z. Lin and Z. S. Yu, Discontinuous Galerkin spectral element lattice Boltzmann method on triangular element, *Int. J. Numer. Methods Fluids*, 42 (2003), 1249–1261.
- [15] X. D. Niu, C. Shu and Y. T. Chew, A lattice Boltzmann BGK model for simulation of micro flows, *Europhys. Lett.*, 67 (2004), 600–606.
- [16] X. K. Ku and J. Z. Lin, Numerical simulation of the flows over two tandem cylinders by lattice Boltzmann method, *Mod. Phys. Lett. B*, 19 (2005), 1551–1554.
- [17] Z. S. Yu and X. M. Shao, A direct-forcing fictitious domain method for particulate flows, *J. Comput. Phys.*, 227 (2007), 292–314.
- [18] R. Glowinski, T. W. Pan, T. I. Hesla and T. T. Joseph, A distributed Lagrange multiplier/fictitious domain method for particulate flows, *Int. J. Multiphase Flow*, 25 (1999) 755–794.
- [19] E. A. Fadlun, R. Verzicco, P. Orlandi and J. Mohd-Yusof, Combined immersed-boundary finite-difference methods for three-dimensional complex flow simulations, *J. Comput. Phys.*, 161 (2000), 35–60.
- [20] Z. G. Feng and E. E. Michaelides, The immersed boundary-lattice Boltzmann method for solving fluid-particles interaction problems, *J. Comput. Phys.*, 195 (2004), 602–628.
- [21] Z. G. Feng and E. E. Michaelides, Proteus: a direct forcing method in the simulations of particulate flows, *J. Comput. Phys.*, 202 (2005), 20–51.
- [22] X. D. Niu, C. Shu, Y. T. Chew and Y. Peng, A momentum exchange-based immersed boundary-lattice Boltzmann method for simulating incompressible viscous flows, *Phys. Lett. A*, 354 (2006), 173–182.
- [23] X. Shi and S. P. Lim, A LBM-DLM/FD method for 3D fluid-structure interactions, *J. Comput. Phys.*, 226 (2007), 2028–2043.
- [24] A. Dupuis, P. Chatelain and P. Koumoutsakos, An immersed boundary-lattice-Boltzmann method for the simulation of the flow past an impulsively started cylinder, *J. Comput. Phys.*,

- 227 (2008), 4486–4498.
- [25] D. Wan and S. Turek, An efficient multigrid-FEM method for the simulation of solid-liquid two phase flows, *J. Comput. Appl. Math.*, 203 (2007), 561–580.
 - [26] S. M. Nicos and D. M. Raymond, Velocity Verlet algorithm for dissipative-particle-dynamics-based models of suspensions, *Phys. Rev. E*, 59 (1999), 3733–3736.
 - [27] Q. Spreiter and M. Walter, Classical Molecular Dynamics Simulation with the Velocity Verlet Algorithm at Strong External Magnetic Fields, *J. Comput. Phys.*, 152 (1999), 102–119.
 - [28] J. Happel and H. Brenner, *Low Reynolds Number Hydrodynamics*, Prentice-Hall, New York, 1965.
 - [29] Z. L. Guo, C. G. Zheng and B. C. Shi, Non-equilibrium extrapolation method for velocity and pressure boundary conditions in the lattice Boltzmann method, *Chin. Phys.*, 11 (2002), 366–374.
 - [30] R. Glowinski, T. W. Pan, T. I. Hesla, D. D. Joseph and J. Periaux, A fictitious domain approach to the direct numerical simulation of incompressible viscous flow past moving rigid bodies: application to particulate flow, *J. Comput. Phys.*, 169 (2001), 363–426.
 - [31] Z. L. Wang, J. R. Fan and K. Luo, Combined multi-direct forcing and immersed boundary method for simulating flows with moving particles, *Int. J. Multiphase Flow*, 34 (2008), 283–302.
 - [32] M. Uhlmann, An immersed boundary method with direct forcing for the simulation of particulate flows, *J. Comput. Phys.*, 209 (2005), 448–476.